Method for Dynamically Detecting Secretions from Single Cells Using a Nanopore

Eamonn Kennedy,[†,§] Mohammad Hokmabadi,[†,§] Zhuxin Dong,[†] Kim McKelvey,[†] Edward M. Nelson,[†] and Gregory Timp*[,‡]

[†]Department of Electrical Engineering and [‡]Department of Electrical Engineering and Biological Science, University of Notre Dame, Notre Dame, Indiana 46556, United States

S *Supporting Information*

ABSTRACT: Secreted proteins mediate cell-to-cell communications. Thus, eavesdropping on the secretome could reveal the cellular phenotype, but it is challenging to detect the proteins because they are secreted only in minute amounts and then diluted in blood plasma or contaminated by cell culture medium or the lysate. In this pilot study, it is demonstrated that secretions from single cancer cells can be detected and dynamically analyzed through measurements of blockades in the electrolytic current due to single molecules translocating through a nanopore in a thin inorganic membrane. It is established that the distribution of blockades can be used to differentiate three different cancer cell lines (U937, MDA-MB-231, and MCF-7) in real time and quickly (<20 s). Importantly, the distinctive blockades associated with the chemokine CCL5, a prognostic factor for disease progression in breast cancer, along with other low-mass biomarkers of breast cancer (PI3, TIMP1, and MMP1) were identified in the context of the secretome of these three cell types, tracked with time, and used to provide information on the cellular phenotype.

KEYWORDS: *Molecular diagnostics, nanopore, single-molecule spectroscopy, protein discrimination, cell phenotype*
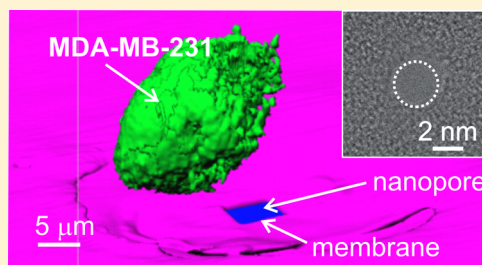
About 16% of human genes are predicted to produce at least one secreted protein.[1] The proteins secreted from a cell, namely the secretome, define the phenotype, and mediate cellular function or signal dysfunction and, thus, show the prospect of revealing biomarkers and targets for drug discovery.[2−8] In particular, secreted proteins play a pivotal role in cancer progression and metastasis by orchestrating migration and invasion. Thus, the secretome may offer signatures of a metastatic phenotype, but it is challenging to detect them because the proteins are secreted only in minute amounts and then diluted in blood plasma or contaminated by cell culture medium or the lysate. Moreover, because a tumor is heterogeneous and exhibits distinct phenotypes, it is necessary to detect a metastatic signature from single cells. Thus, sensitivity is paramount.

Currently, mass spectrometry (MS) is used prevalently for protein analysis, but this method lacks the sensitivity required for single cell secretomics.[4−12] Specifically, due to their high biological activity, the concentration of low-molecular-weight cytokines in extracellular fluids is so dilute (usually in low-picomolar concentrations) that they are practically undetectable by proteomic profiling based on MS.[4,6,8,9,11] Only a few pioneering studies have profiled secreted proteins, and most were accomplished at a bulk-culture level. Tissue heterogeneity is subsumed by bulk culture analyses accomplished with MS or enzyme-linked immunosorbant assay, however. A few studies have scrutinized single cells with MS,[5,7] but they were not very sensitive (less than femtomoles). Assays such as multiple

reaction monitoring and antibody-based enrichment used in conjunction with MS offer improved sensitivity to peptides with a priori knowledge of the target,[10−12] but the limit of quantification is usually a low concentration of nanograms per milliliter, which still translates to more than a billion copies.

However, there are several methodologies that can purportedly measure secretions from single cells, including serial analysis of gene expression, DNA microarrays, antibody arrays such as single cell bar-code chips (SCBC), and RNA sequencing.[3,5,7] These all have advantages and disadvantages, but most do not afford the opportunity for real-time detection, and none offer single-cell selectivity with single-molecule sensitivity. For example, one of the disadvantages of single-cell RNA sequencing is that the proteins are not measured directly. Instead, the reads over-represent the most-abundant RNAs, leading to identification of only the most common proteins. Deep (high coverage) sequencing is required for rare transcripts, but then the amplification, selection, and hybridization required for single-cell analysis yield uneven coverage, noise, and inaccurate quantification.[4] Finally, the cell is destroyed in the process. However, SCBC suffers from limitations common to immunoassays.[3] It uses microfluidic devices to measure secretions from single cells, relying on immune-reactions between patterned antibodies and/or
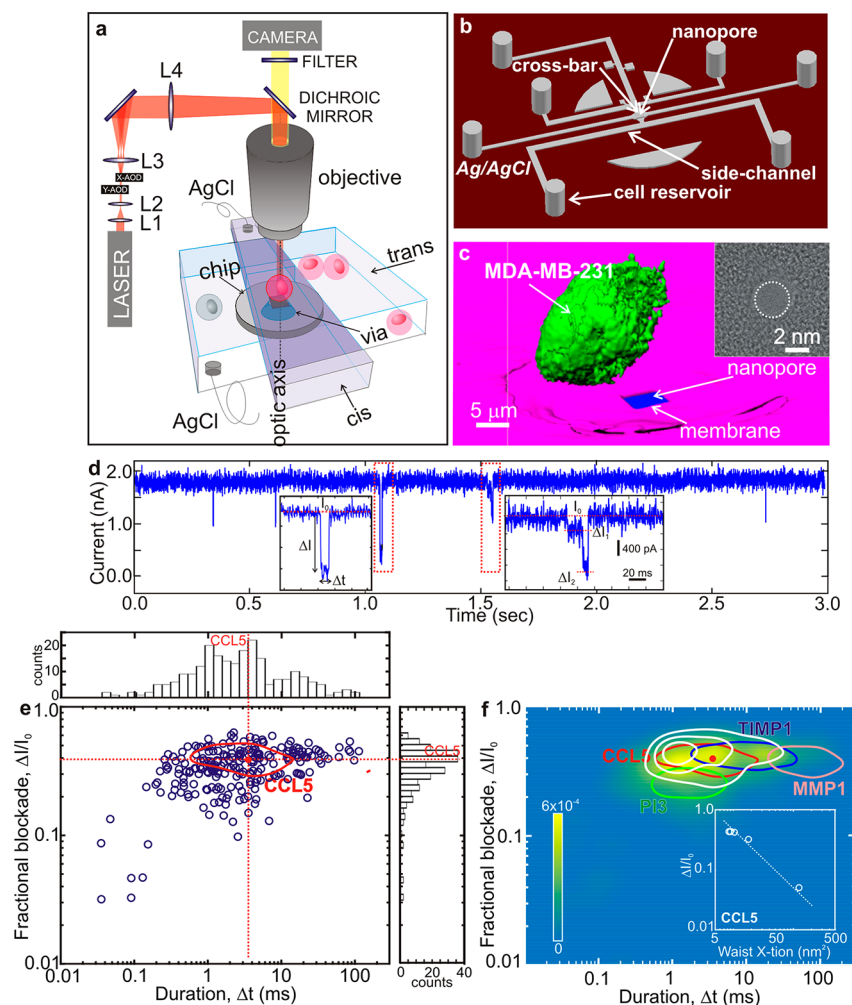
Figure 1. Detecting secretions from a single cell. (a) A schematic of the microfluidic cell conveyer and optical tweezers is shown. Cells were manipulated using optical tweezers formed by focusing infrared light (red path) from a Ti:sapphire laser through a commercial optical microscope with a high NA objective. The same optics were used for imaging (yellow path). (b) A drawing of the seven-port microfluidic device with a nanopore embedded in the cross-bar is shown. The cells were conveyed from a reservoir via the side-channel to the cross-bar using optical tweezers in conjunction with a pressurized flow. (c) A false-color (perspective) reconstruction is shown of an MDA-MB-231 cell (green) suspended over a silicon nitride membrane with a nanopore in it. The reconstruction was formed from volumetric confocal fluorescence data. The blue channel measured the excitation laser's scattering without an excitation filter, indicating the position of the membrane. Inset: a transmission electron micrograph (TEM) of a (2.8 nm × 2.9 nm →) 6.4 nm^2 cross-section nanopore is shown; the shot noise highlighted by the dashed circle delineates the pore. (d) A typical current trace is shown that illustrates the distribution of blockade fractions and durations acquired from a U937 cell suspended about 5 μm above a nanopore measured at −0.70 V bias. Insets: a magnified view of the signal highlighted in red delineates the open pore current (I_0), blockade (ΔI), and the duration (Δt) for single and multilevel blockades. (e) The distribution of fractional blockades ($\Delta I/I_0$) vs the blockade duration (Δt), acquired from a pore with a 6.4 nm^2 cross-section for a single U937 cell, is shown. The data was multivariate, as is evident from the fractional blockade current and duration histograms (top and right panels). For comparison, a red contour that captures 0.50 (50%) of the fractional blockade distribution acquired from a pure solution of CCL5 is juxtaposed on the data. (f) PDF heat-map of the blockade distributions plotted in panel e is shown. For comparison, 0.25, 0.50, and 0.75 contours characterizing another U937 cell measured under the same conditions are juxtaposed on the heat map. The corresponding Cramér's distance (Δ) between the two U937 cells shown is $\Delta = 6.1 \times 10^{-5}$. Also for comparison are contours that capture 0.50 of the fractional blockade distributions acquired from pure solutions of PI3, CCL5, TIMP1 and MMP1 juxtaposed on the data. Inset: the median fractional blockade acquired from pure 100 pM solutions of CCL5 is shown as a function of the pore cross-sectional area at the waist. The median fractional blockade scales nearly linearly (dashed line) with the cross-section.

antigens to identify aspects of the secretome. The availability of a specific antibody is critical to such methods, but antibodies are costly to synthesize, and only a limited number of antigens can be analyzed this way. Poor specificity can lead to low sensitivity. The detection limit is supposed to be greater than 100−1000 copies, but it is plagued by nonspecific binding to the antibodies and false negatives due to the Prozone effect, and the proteins must be identified a priori for analysis. Finally, a method for assaying a single cell is absent, which is especially relevant for assays of precious primary cells; sometimes two or

three cells are assayed together, and sometimes none are. What is needed is an extremely sensitive method for directly measuring secretions from a single cell without destroying it.

In this pilot study, a practical method is demonstrated for detecting and dynamically analyzing secretions from single cancer cells through measurements of blockades in the electrolytic current due to single molecules translocating through a nanopore in a thin inorganic membrane. To read the secretome, a single cell is positioned with optical tweezers over a nanopore embedded in a microfluidic device, and it is

held there while secretions diffuse up to the pore and are impelled through it by an electric field. Because the blockade currents are a measure of the occluding molecular volumes, a nanopore can prospectively discriminate by volume the proteins in the secretome of a single cell without a priori knowledge or compromising cell viability. Because it provides information on the phenotype in this way, it is argued that the distribution of blockades can be used to differentiate between cell types, even if only a limited aspect of the secretome is actually measured. Importantly, if the proteins can be discriminated by volume, then the blockades associated with prognostic factors can be identified in the context of the secretome. Finally, a numerical method is demonstrated that can be used to track a particular molecular secretion and so provide information on the phenotype in real time.

Results and Discussion. The distinctive blockades that develop in the ionic current through a nanopore when a charged molecule is impelled through it by an electric field have been used to analyze native and denatured protein in pure solutions before[13−17] but not within a complex milieu like the secretome. To measure the secretions from a single cell, several technical obstacles had to be overcome. First, because the concentration was so dilute, the secretome could easily be contaminated by proteins found in the suspension. Thus, the cells had to be well-isolated, which further implied that biofouling of the microfluidic device by protein and adherent cells had to be practically eliminated. Second, the yoctoliter-scale volume of electrolyte in the nanopore that confers single molecule sensitivity also made it prone to fouling if the protein adhered to the membrane. If it was fouled, the membrane supporting the nanopore had to be resilient enough to withstand chemical denaturation agents, such as NaOCl (bleach)[18] or the high electric fields used to clear it.[19] Third, because the electric field extended above the pore, to avoid electroporation,[20] the cell had to be positioned out of range of this field, and so, a micrometer-size gap between the cell and the pore was indicated (Figure S1). Finally, because the nanopore acquired secretions primarily by diffusive transport across the micrometer-size gap, the acquisition time becomes a factor in the data collection.

To overcome these obstacles, an experiment was configured that used a nanopore through a silicon nitride membrane embedded in a microfluidic device (see Figure 1a and the Methods in the Supporting Information). The silicon chip supporting the membrane was embedded in the cross-bar of a seven-port microfluidic device that provided direct electrical, fluidic, and optical access to the pore (Figure 1b). Devices without fouling-resistant coatings[21] were frequently employed because of their resilience to the bleach and acids used to rehabilitate the pore. When the nanopore was fouled by protein, it was cleared by reversing the applied voltage, by flushing (10−50 μL/min) both the cis and trans sides of the membrane with phosphate buffered saline (PBS) or 18 MΩ deionized water, or both. When this failed, the cis side of the membrane was exposed to a 0.5−1% solution of NaOCl or 1 M HCl for 5−60 s to cause proteins to unfold and then repeatedly flushed with PBS until the open pore conductance recovered (Figures S2 and S3).

Optical tweezers were used to position the cell over a nanopore and hold it there for analysis (Figure 1c). Optical tweezers offered a benign strategy for manipulating cells with high precision.[20,22] Long-duration (3 min) exposures were possible at a wavelength of 900 nm with tolerable viability

(∼90%; see the Supporting Information and Figure S4). Finally, to avoid contamination, a cell suspension (in medium) was introduced into a reservoir in the microfluidic device >1 mm away from the pore, and then cells were flowed under pressure at 10−20 μm/s through a side-channel to a cross-channel within 500 μm of the pore (Figure 1b). While the volume over the pore was continuously flushed with another flow of 1× PBS, a single cell was extracted from the main flow using optical tweezers and pulled through the cross-channel upstream, against the flow of PBS, toward the pore until finally, the centroid of the cell was positioned about 10 μm from the center of the membrane where the pore was located (Figure 1c). Even in the absence of flow over the pore, there was a protein concentration gradient between the cell and the pore (Figure S5).[23]

As a crucible for testing the method, three different cell-lines were assayed; two of them are commonly used as in vitro models for breast cancer.[24] The first was the breast cancer cell-line MDA-MB-231 that has a negative estrogen receptor (ER−), a negative progesterone receptor (PR−), and a negative human epidermal growth factor receptor-2 (HER-2−) profile. The status of ER, PR, and HER-2 correlates with carcinogenesis and the progression of neoplasms. In particular, the triple negative status of cell-lines such as MDA-MB-231 is associated with an invasive, metastatic form of cancer with a miserable prognosis. The second cell-line, MCF-7, has an ER+, PR+, and HER-2± profile that is more indolent than MDA-MB-231. It is less invasive with a lower metastatic potential and is associated with low-grade, luminal "A" cancers with the best prognosis. The third cell type, U937, a human lymphoma cell, was used as a control because it secretes a large number of cytokines and chemokines.[25]

When a cell was placed in close proximity, the nanopore furnished electrical signatures for it almost immediately, i.e., transients were observed in the ionic current, some of which were blockades. To facilitate comparisons between cells, the data were collected until a similar number of blockade counts were tallied at a voltage bias of −0.70 V, which forced positively charged proteins through the pore. Under these conditions, when a cell was positioned over a pore with an elliptical (2.8 nm × 2.9 nm →) 6.4 nm^2 cross-section (Figure 1c, inset), transients in the open pore current were observed at a rate of about 1 blockade per second (Figure 1d), whereas practically no transients were observed in the absence of a cell above the noise (Figure S3). Under these conditions, the subset of transients that were blockades were associated with trans-locations of a molecule through the pore.[15,19] These were classified according to the change in the pore current measured relative to the open pore value, $\Delta I/I_0$, and its duration, Δt (Figure 1d, left inset). Typically, >85% of the blockades were categorized as single-level transients (Figure 1d, left inset), but long-duration (>10 ms) multilevel transients were also observed (Figure 1d, right inset). The histogram technique, used prevalently for the analysis of pore currents, classified the blockades using a threshold determined from maximum likelihood estimates,[26] and performed well for low-noise signals and single-level transients (Figure S6). However, multilevel events, which were interpreted to represent either a trans-location that was sterically hindered or a molecule reorientating as it transited the pore[27] or multiple proteins competing for the pore at the same time, required a more sophisticated analysis.

The compiled distributions of blockades were evidently multivariate[28] (which followed from the histograms) and

depended on the pore topography (as was apparent from a comparison of Figures 1e,f and S7a,b), and on the arrival time (see Figure S8). In particular, the data acquired from a U937 cell, using a pore with a (12.1 nm × 12.8 nm →) 122 nm^2 cross-section at the waist yielded more transients per second (2757 blockades were acquired in 17 min, or 2.7 blockades per second) and a disproportionately broader spectrum of blockade fractions and durations compared to that acquired with a pore with a smaller, a 6.4 nm^2 cross-section at the waist (229 blockades were acquired in 3 min, or 1.3 blockades per second).[15] Because the number of blockades comprising each of the distributions was variable, to compare different cells, the aggregate data were generally depicted as normalized heat maps of the probability density functions (PDF; Figure 1f).

From these data, we formed the hypothesis that the blockade distribution represented selective aspects of the secretome of a cell. It is selective because, as the pore diameter approaches the hydrodynamic diameter of the protein, the mobility collapses and so the blockade duration increases (1000- to 10 000-fold)[29] until, eventually, the molecule fails to permeate through the membrane at all. It followed then that the larger pore likely reflected a more comprehensive snapshot of the secretome over time with the coverage (defined as the percentage of unique secretome proteins that could blockade the pore at least once) limited by the number of blockades tallied, the signal-to-noise ratio (SNR), and bandwidth.[15,30] To appreciate the former limitation, the fraction of the secretome observed was estimated from the number of blockades, ignoring the variable species concentration, collection efficiency, and protein gradients (Figure S9a). On the one hand, a 3 min data acquisition window for the pore with a 6.4 nm^2 cross-section produced about ($p =$) 200 blockades, so that only about 6% of the whole secretome could be assessed at maximum at least once. However, only about 8% of the entire secretome was likely to permeate the small cross-section of the pore (Figure S9b), and so the observable number is even smaller. On the other hand, for a 17 min window, the pore with a 122 nm^2 cross-section yielded about 2800 blockades, corresponding to about 65% of unique secretions observed once, which compared favorably to the estimated 9000 blockade minimum required for a comprehensive sampling of the whole secretome of a human cell that was estimated to consist of about 3500 proteins.[1] Accordingly, an acquisition window of more than an hour would be required to cover the secretome comprehensively.

According to measurements of pure protein (control) solutions, the limitations imposed by the SNR and bandwidth hardly affected the measurement of the fractional blockade current and duration, likely because the nanopore cross-section was so much smaller than those used in similar work reported earlier.[15,31] Naïvely, the fractional change in the blockade current, $\Delta I/I_0$, was supposed to inform on the molecular volume according to $\Delta I/I_0 = f \cdot \Delta V_{mol}/V_{pore} \cdot S$, where f is a gauge of the molecular shape and orientation; ΔV_{mol} and V_{pore} denoted the molecular volume in the pore and the pore volume, respectively; and S is a size factor that accounts for distortions in the electric field that occur when the molecule is comparable in size to the pore.[16,27] Likewise, the duration of the blockade, Δt, was supposed to be an important signature and, under certain circumstances, represented a measure of the molecular length.[16] So, it was argued that the PDFs reflected the volumes of the different molecular constituencies in respective secretomes.

As an illustration, the heat maps of U937-PDFs were juxtaposed with contours enclosing 0.50 (50%) of the respective distributions associated with pure (100 pM) protein controls, including the mature elafin, a protease inhibitor (PI3, molecular weight [MW] = 6.0 kDa); RANTES, the mature C−C motif chemokine 5 (CCL5, MW = 7.8 kDa); a glycoprotein that acts like a metallopeptidase inhibitor (TIMP1, MW = 28.5 kDa); and matrix metalloproteinase-1 protein (MMP1, MW = 54.0 kDa), which have all been identified as prognostic factors in breast cancer (Figure 1f and S10).[25,31−34] The juxtaposition indicated that cell secretions in the range from 6.0 kDa (PI3) to 54.0 kDa (MMP1) could easily be detected and discriminated on the basis of the fractional blockade and the blockade duration observed using a pore with a 6.4 nm^2 cross-section at the waist. The aggregate of fractional blockade distributions derived from these four proteins spanned most of the U937 blockade distribution, extending from 0.12 < $\Delta I/I_0$ < 7 and 0.12 < Δt < 100 ms. The juxtaposition of the CCL5 contours on the heat maps of U937-PDFs (Figures 1f and S7b; red contours) was consistent with the possibility that CCL5 could be detected for pores with cross-sections ranging from 6.4 to 122 nm^2. Importantly, the pore with the smaller (6.4 nm^2) cross-section pushed the CCL5 distribution to higher fractional blockades and longer durations overall, closer to the medians of the distribution, which improved the SNR and temporal resolution relative to a pore with a larger cross-section (122 nm^2; see Figure S7). This suggested that molecules with a volume similar to CCL5 predominated in the distribution acquired from the smaller pore.

Based on this evidence, it was reasoned that the pore waist must act like a selective, spatial filter through which only proteins with a commensurate size or smaller could permeate.[29] If the molecular weight of a secretion scales approximately with the volume according to[35] V_{mol} (nm^3) = 1.21 × 10^{-3} × MW (Da), then (spherical) proteins with MW of <0.84 MDa would permeate a pore with a 122 nm^2 cross-section, which covers almost the entire human secretome, in principle, whereas only proteins with a MW of ≤10 kDa would permeate the pore with a 6.4 nm^2 cross-section. It followed that proteins larger than the pore waist might still be detected but would likely denature to translocate across the membrane,[13,14,36] forcing an extended blockade duration and producing a fractional blockade that was unrepresentative of the native protein structure. This seemed like a plausible explanation for the 100-fold extension of the blockade duration associated with MMP1 compared to PI3 acquired with the small pore. Thus, it seemed likely that only select constituents of the secretome were detected by the pore with the smaller cross-section at the waist.

To test this idea further, the median fractional blockades acquired from a pure solution of CCL5 using pores with different cross-sectional areas were measured. Because CCL5 is prone to aggregation and oligomerization,[37] the volumes of a monomer, dimer, and tetramer were calculated using a Monte Carlo (MC) simulation[38] and then hydrated[39] and recalculated (Figure S11 and Methods). These calculations yielded volumes of 15.3 nm^3 (49.2 nm^3), 28.4 nm^3 (97.8 nm^3), and 55.3 nm^3 (182 nm^3) for the unhydrated (hydrated) monomers, dimers, and tetramers of CCL5, respectively (Table S1). To validate the calculations, the molecular volumes of CCL5 oligomers were also measured directly with AFM and compared with fractional blockade currents (Figure S12). Following the erosion of the image to account for the shape of the AFM tip, at least three volumes were apparent in the AFM data:
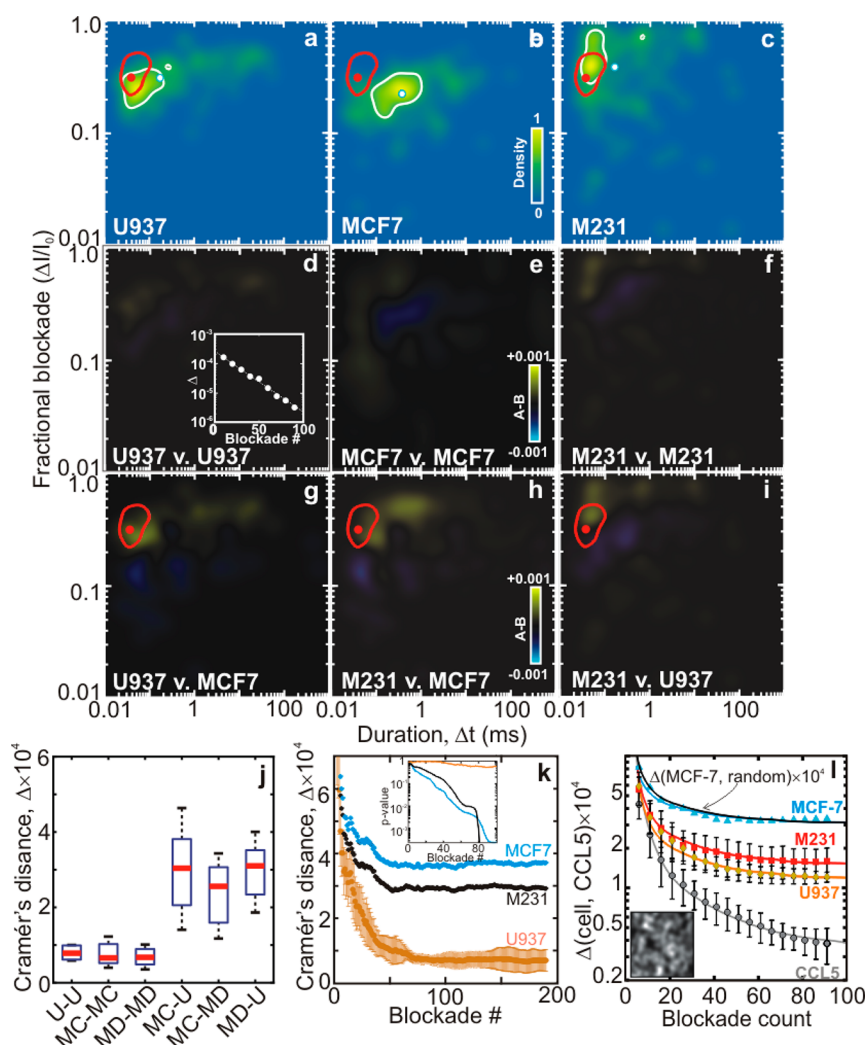
Figure 2. Comparison of secretions from three different cancer cell types. (a–c) Representative PDF heat maps of the blockade distributions spanned by the fractional blockade ($\Delta I/I_0$) and the blockade duration (Δt) are shown, which were acquired from individual U937, MCF-7, and MDA-MB-231 cells, respectively, using the same nanopore with a ($3.7\ \text{nm} \times 4.1\ \text{nm} \rightarrow$) $12.3\ \text{nm}^2$ cross-section at -0.60 V. The heat maps represent 86, 95, and 116 blockades, respectively. The white contours juxtaposed on the maps capture 0.50 (50%) of the cell distribution. For comparison, the red contours that capture 0.50 of the distribution acquired from a pure solution of CCL5 using the same pore are juxtaposed on the same maps. (d–f) Heat maps are shown that show the difference between PDFs acquired from two individuals from the *same* cell types, i.e., U937 versus U937, MCF-7 versus MCF-7, and MDA-MB-231 versus MDA-MB-231, respectively. The differences between similar cell types were miniscule. (d, inset) The Cramér's distances (Δ) calculated from distributions taken from the same cell are shown as a function of the number of blockades acquired from it. (g–i) Like panels d–f, but illustrating the differences between PDFs, acquired using the same pore from *different* cell types, i.e., U937 vs MCF-7, MDA-MB-231 vs MCF-7, and MDA-MB-231 vs U937, respectively. (j) Box-and-whisker plots are shown of Δ, compiled from 74 individuals of the same and different cell types. A comparison of different cell types yields a 3-fold larger Δ in comparison to similar cell types. (k) The distances Δ calculated between a compilation of U937 cells (U937 orange, control) versus individuals from the two other cancer cell-lines (MDA-MB-231, black; and MCF-7, blue) are shown as a function of blockade count. To account for phenotypic diversity, five U937s comprised the population used for comparison, to establish the standard deviation of Δ (orange error bars). Within <20 blockades, each cell line could be classified. (k, inset) The p value is shown, which represents the (calculated) probabilities for observing a U937 for each cell type as a function of blockade count. Whereas the true observation, p(U937), remained near 100% likelihood for all U937 cells (orange line), in contrast, both MDA-MB-231 [p(M231)] and MCF-7 [p(MCF7)] were rejected as U937 with $p > 99.9\%$ for counts of 80 blockades and above. (l) The distances Δ calculated between the three cell types (U937 orange diamonds, control; MCF-7, blue triangles; and MDA-MB-231, red squares) vs CCL5 (gray circle) are shown as a function of blockade count. (l, inset) A heat map of the randomized distribution used for comparison to MCF-7 (solid black line).

V_{CCL5} = 53.3 ± 3.2, 99.2 ± 19.3, and 209.9 ± 8.6 nm^3, where the error denotes the width of the Gaussian fits. Based on this assessment, it was assumed that the molecular volume of the unhydrated monomer (dimer and tetramer) was $\Delta V_{\text{CCL5}} = 15.3$ nm^3 (28.4 and 55.3 nm^3).

Next, to calculate the fractional blockade current corresponding to the CCL5 oligomers, the effective pore volume was estimated using finite element simulations (FES). The effective

thickness of the membrane, defined by the electric field (full-width at half-maximum), was estimated to be about 4 (8) nm for membranes nominally 10 (30) nm thick, and so the corresponding effective pore volume was calculated to be about 35 nm^3 (1350 nm^3) for the pore with the 6.4 nm^2 (122 nm^2) cross-section, assuming a biconical pore with a 15° (<30°) cone angle (see Supplemental Note 1, Table S2, and Figure S13).[40] Therefore, a naïve estimate for the fractional blockade due to

the CCL5 monomer in the pore with the 6.4 nm^2-cross-section was $\Delta V_{CCL5}/V_{pore}^{eff} = 15.3/36.2 = 0.42$, which coincided with the measured median $\Delta I/I0 = 0.40$. This estimate ignores effects associated with the pore and protein charges and distortions in the electric field or protein conformation as the molecule translocated through the pore, for example. However, the median blockade associated with the pure CCL5 solutions scaled linearly with the cross-sectional area of the pore waist (Figure 1f; inset), and so it was inferred that the median blockade current, derived from measurements of pure solutions of the protein was commensurate with the size of unhydrated CCL5.

It was reasoned that, if a nanopore can actually be used to interrogate selective aspects of the secretome, then the PDFs acquired from cells of the same type should be essentially similar, whereas PDFs from different cell types would be distinct. As a preliminary test of this proposition, the contours characterizing the data acquired from another U937 cell under the same conditions were superimposed on the heat-map of the first (white contours in Figure 1f). Although the heat-map coincided with the contours generally, subtle differences were perceived between the two otherwise identical cells. So, for a more-rigorous test, data were acquired from individuals representing the three dissimilar cell types and then cross-correlated.

A typical example is represented in Figure 2a−c, in which the same nanopore with a $(3.7 \text{ nm} \times 4.3 \text{ nm} \rightarrow)$ 12.3 nm^2 cross-section was used to acquire data from individuals from each cell type. To quantify the differences, the PDFs were subtracted, point-by-point, i.e., $(\text{PDF}_{P_1} - \text{PDF}_{P_2})$, to create difference maps (Figure 2d−i), the elements of which were squared and summed to produce a measure of the statistical distance between the two probability distributions called the Cramér's distance, Δ (see the Methods in the Supporting Information).[28] Because the logarithm of the Cramér's distance was found to be linearly related to the number of blockades (Figure 2d, inset), for a (lower bound) rate of about 0.5 s^{-1} and a maximum error of 10%, it was estimated that a 3 min acquisition window (or about 90 blockades) would be sufficient to discriminate between cell types.

In toto data were collected using multiple pores with cross-sections ranging from 6.4 to 12.3 nm^2 from 74 cells: 25 U937, 21 MDA-MB-231, and 28 MCF-7. Only data acquired from pores with practically identical cross-sections at the waist were compared, which means that the data fell into one of three categories associated with pores with either 6.4 ± 0.4, 9.9 ± 0.4, or 12.3 ± 0.4 cross-sections at the waist. On the one hand, for individuals of the same U937 cell type, the Cramér's distance was $\Delta_{U937} = 7.8 \times 10^{-5}$, on average, whereas for MCF-7, $\Delta_{MCF7} = 6.7 \times 10^{-5}$, and for MDA-MB-231, $\Delta_{231} = 6.7 \times 10^{-5}$ (Figure 2j, left). On the other hand, the Cramér's distances between dissimilar cells were at least 3-fold higher, i.e., $\Delta = 30.6 \times 10^{-5}$, between U937 and MCF-7, on average; $\Delta = 25.7 \times 10^{-5}$, between MDA-MB-231 and MCF-7; and $\Delta = 31.3 \times 10^{-5}$, between MDA-MB-231 and U937 (Figure 2j, right).

Thus, using the Cramér's distance, the cell type could generally be discriminated. For example, using the criterion of $\Delta = 15.0 \times 10^{-5}$, 143 out of 152 (94.1%) pair-wise comparisons were correctly classified; the incorrect classifications associated with U937 and MCF-7 may just reflect phenotype diversity within a monoculture.[41] Moreover, dissimilar cell types could be resolved without ambiguity with as few as 20 blockades

(Figure 2k). Assuming a typical interarrival time of about 1 s, cells from each cell type could be classified in less than 20 s. In particular, the p value representing the probabilities for observing a U937 remained at nearly 100% likelihood for all U937 cells [p(U937) in Figure 2k inset], whereas, in contrast, both MDA-MB-231 [p(M231)] and MCF-7 [p(MCF7)] were rejected as U937 with $p > 99.9\%$ for counts of 80 blockades and above.

The distinctiveness revealed by the Cramér's distance was attributed to the different molecular constituencies, their concentrations in the respective secretomes, or both. For corroboration, the blockade distribution, amassed from a pure solution of CCL5 using the pore with the 12.3 nm^2 cross-section, was compared with the blockade distributions associated with the three cell types (Figure 2a−c, red contours) using Δ as a metric (Figure 2l). CCL5 represented a suitable choice because it is a constituent of the secretome of all three cell types.[31,32] From this assessment, it was inferred that the CCL5 and MCF-7 distributions had few common features because MCF-7 (triangle) and a randomized distribution (Figure 2l, solid line and inset) produced practically the same result. However, the distributions of both U937 (diamonds) and MDA-MB-231 (squares) and CCL5 were more alike, but imperfectly so, as gauged by the self-similarity of CCL5 (circles).

This inference obliged us to examine more closely the regions of interest (ROI) in the blockade distributions of the three cell types (Figure 2a−c, red contours) and their differences (Figure 2g−i), defined by the domain of the CCL5 distribution. Interestingly, a hot spot was conspicuous in both the cell types and in the difference maps, which was nearly coincident with the molecular volume of CCL5. (The ratio of the molecular volume of CCL5 to the pore volume for this pore was estimated to be $\Delta V_{CCL5}/V_{pore}^{eff} = 15.3/62 = 0.25$, which was similar to the measured median of the pure CCL5 solution, $\Delta I/I_0 = 0.32$; see Figure S14). Moreover, although the specific location within the blockade distributions and difference maps was forced to change by using different nanopore topographies, the coincidence between hot-spots in the difference maps and distributions acquired from dilute pure solutions of CCL5 persisted (Figure S15). Generally, integration over the ROI in the blockade distributions and difference maps, defined by the area encompassed by a CCL5 contour, indicated that MDA-MB-231 secreted molecular volumes were consistent with CCL5-like blockades in excess of MCF-7 and likewise for U937 compared to MCF-7, at least up to the 0.70 contour (Figure S16). However, the MDA-MB-231 secretions were comparable with those from U937 because the integrated difference between the pair over the area of the contour nearly vanished, at least up to the 0.60 contour. (Integration over an ROI defined by contours extending beyond 0.80 were untenable due to false positives [see Figure S3] and the paucity of data there.) These data indicated higher constitutive expression of CCL5 from U937 and MDA-MB-231 relative to MCF-7 cells (Figure S16; inset), which was consistent with real-time qualitative polymerase chain reaction (RT-qPCR) results obtained from bulk cultures (Figure S17) but contradicted prior work.[42]

The inference that the blockade distribution can inform on the expression of a specific protein was supported directly by two additional observations: (1) the consonance between hot-spots in the blockade distributions extracted from MDA-MB-231 cells engineered to express CCL5 and a pure solution of CCL5 and (2) the correlation between the level of expression
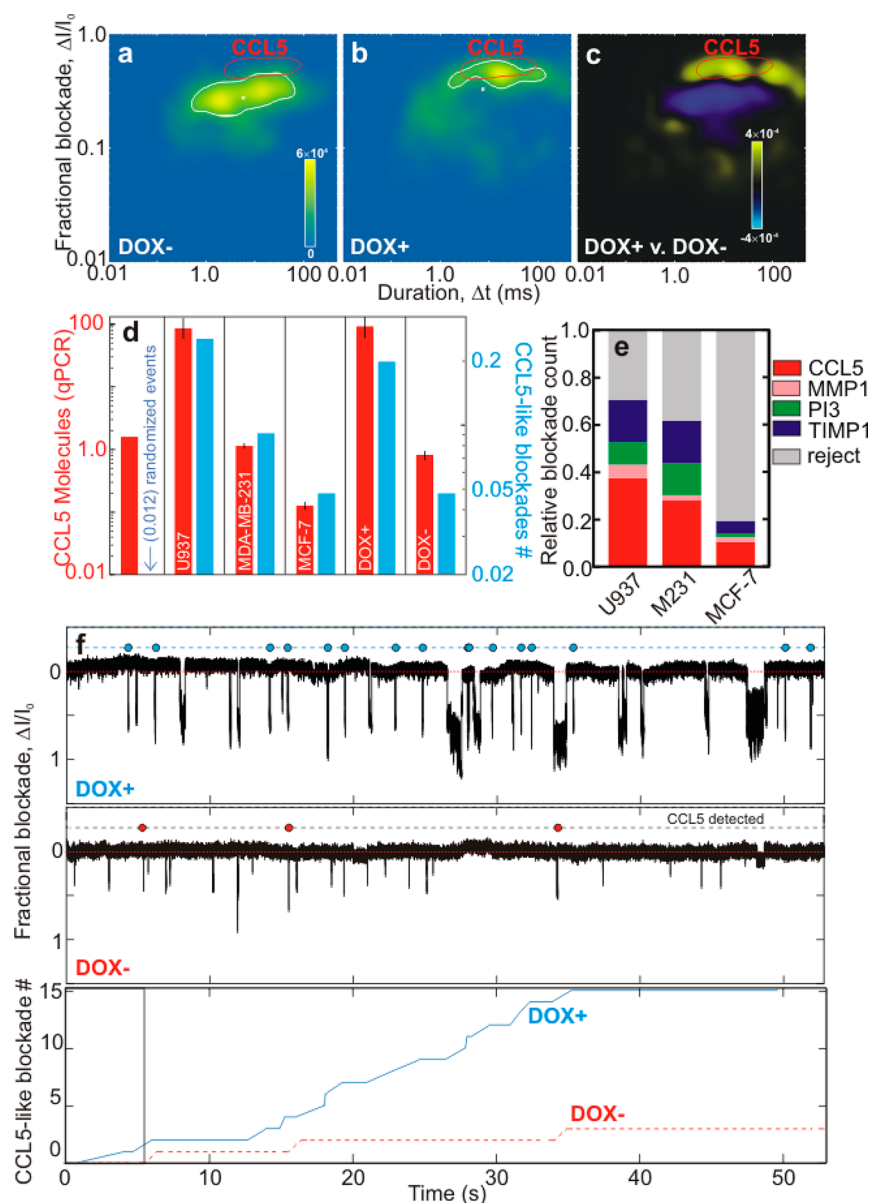
Figure 3. Biomarker gene expression in the secretome of cancer cells. (a,b) Heat maps of the PDFs representing aspects of the secretome of an engineered MDA-MB-231 cancer cell line are shown without and with induction (DOX− and DOX+), respectively, acquired using a pore with a (2.0 nm × 3.6 nm →) 5.7 nm^2 cross-section at −0.60 V. The heat maps for DOX− and DOX+ represent 234 and 259 blockades. The white contour lines capture 0.50 (50%) of the cell distributions, whereas the red contours capture 0.50 of the distribution acquired from pure solutions of CCL5. (c) The difference between the PDFs of the DOX+ and DOX− distributions (PDF$_{DOX+}$ − PDF$_{DOX−}$) is juxtaposed with a 0.50 (red) contour characterizing the blockade distribution acquired from CCL5. Surplus CCL5-like blockades are indicated in the DOX+ distribution. (d) A pair of sets of bar-graphs are shown: one relating the semiquantitative RT-qPCR results for U937, MCF-7, MDA-MB-231 (naïve) and engineered for DOX-inducible CCL5 expression using HPRT as a reference (red; and another alongside it showing the tally of CCL5-like blockades derived from the CCL5 domain identified in the same cells (blue). When CCL5 was subcloned into ptetON and transfected into MDA-MB-231 cells, CCL5 expression was significantly up-regulated in the presence of DOX, becoming comparable to the expression in U937 and overshadowing expression in MCF-7 or DOX. Likewise, the transfection of shRNA against CCL5, reduced the endogenous CCL5 expression by >50%. The correlation between the RT-qPCR and CCL5-like response inferred from the single cell blockade distributions was PCC = 0.95. (e) Bar-graphs are shown that delineate the fraction of secretions attributed to the same four proteins, PI3, CCL5, TIMP1, and MMP1, defined by 0.40 contours, plus unclassified (rejected) proteins all extracted from data such as that shown in Figure S20. (f; top and middle) Typical current traces are shown that illustrate the distribution of blockade fractions and durations acquired from DOX+ and DOX− cells suspended about 5 μm above a pore with a 4.7 nm^2 cross-section, measured at −0.70 V bias. The circles above the traces indicate that CCL5 was detected. (f; bottom) Cumulative CCL5-like blockades are shown for each of the above traces. The CCL5-like tally for DOX+ rapidly (<30 s) outstrips DOX−.

of CCL5 in the three cell types derived from the blockade distributions and bulk RT-qPCR.

One indication that the blockade distribution informed on the level of CCL5 expression was gleaned from a cell-line engineered to up-regulate the molecule. A stable MDA-MB-231

cell-line was constructed using the ptetON system that up-regulated expression of CCL5 in a doxycycline (DOX)-inducible manner, whereas endogenous CCL5 was simultaneously knocked-down by shRNA (see the Methods section in the Supporting Information). Secretions from single cells taken

from the engineered MDA-MB-231 cell line, with and without DOX induction (DOX±), were measured using a pore with a (2.0 nm × 3.6 nm →) 5.7 nm^2 cross-section and effective volume of V_{pore}^{eff} = 33 nm^3 at −0.60 V (Figure 3a,b). Next, a difference-map was formed by calculating PDF$_{DOX+}$ − PDF$_{DOX−}$, which revealed a hot-spot within the 0.50 contour representing data acquired from a pure solution of CCL5 (Figure 3c). Although the pure solution of CCL5 produced a median fractional blockade of $\Delta I/I_0$ = 0.49 that compared favorably to the volume estimate for the CCL5 monomer, i.e., $\Delta V_{CCL5}/V_{pore}$ = 15.3/33 = 0.47 (Figure 3c; red contour), the correspondence between the hot spot in the difference map and the pure solution of CCL5 was imperfect. The difference map may also reflect other changes in the constituents in the secretome of these cells accompanying the up-regulation of CCL5, but ostensibly, it was still possible to measure the expression of a particular molecule in the secretome of a single cell using a nanopore.

More evidence that the blockade distribution informed specifically on CCL5 expression was extracted from bulk RT-qPCR. According to RT-qPCR, 10 min after induction with 10 μg/mL DOX (DOX+), the engineered cell-line showed a 40-fold increase in CCL5 expression relative to wild-type MDA-MB-231, which was comparable to the expression measured in U937 (Figures 3d and S18). However, the level of CCL5 expression in MCF-7 was much lower; it was nearly 800-fold higher in U937. Likewise, wild-type MDA-MB-231 was eclipsed by expression from U937, which was nearly 40-fold higher, consistent with other work,[43] but when shRNA against CCL5 alone was introduced into MDA-MB-231, the CCL5 expression level decreased to 67% of the control that expressed shRNA of a scrambled sequence (Figure S17).

The RT-qPCR outcomes indicated disparities in the levels of CCL5 expression between different cell types in bulk, and so it was reasoned that these disparities should also be reflected in the single cell blockade distributions of the different cell types. To test this assertion, secretions were acquired from MDA-MB-231, MCF-7, and U937 cells using a pore with a (2.1 nm × 3.3 nm →) 5.4 nm^2 cross-section and compared to RT-qPCR. Like the bulk RT-qPCR, the results obtained by integrating the PDFs over a domain defined by a pure solution of CCL5 exhibited strong expression of CCL5-like molecules from both U937 and DOX+, relative to either DOX− or MCF-7; the Pearson correlation coefficient (PCC) indicated that the bulk and single-cell blockade current data were highly correlated, i.e., PCC = 0.95 (Figure 3d). However, the single-cell measurements revealed smaller differences between high and low expression; an increase of only about 4-fold was observed. The smaller differences were ascribed to false positives in the analysis due to the dearth of CCL5-like blockades collected from the MCF-7 and DOX− cells. This argument was bolstered by an analysis that showed that the number of CCL5-like molecules detected from MCF-7 (DOX−) represented only about 10% (17%) of the total number of blockades in the distribution (Figure S18). Together with the control tally used to mimic noise, created numerically from a randomized distribution with the same number of blockades that produced 0.012 CCL5 blockade per second (randomized in Figure 3d) compared to 0.1 blockades per second acquired from U937 and DOX+, it seemed likely that some false positives were erroneously counted. Thus, the highly correlated bulk and single cell data provided yet more proof that a nanopore can be used to interrogate specific aspects of the secretome (in this

case, associated with the molecular volume of a CCL5 monomer).

The power to identify a specific molecular volume kicks open the door to more comprehensive assays that dynamically and simultaneously canvass more than one biomarker (even without a priori knowledge or enrichment of the protein), provided that the nanopore can resolve the differences. As an illustration, data were collected from the three cell types and pure solutions of the four proteins (PI3, CCL5, TIMP1, and MMP1) using nanopores with 6.4−6.6 nm^2 cross-sections at the waist at −0.70 V (Figure 19a−c), and the normalized blockades attributed to each of the proteins, along with a rejected classification, were estimated (Figures 3e and S20).

Naïvely, assuming that these five classes accounted for all the aspects of the secretome detected by a nanopore with this waist, each observation of a blockade ($\Delta I/I_0$ and Δt) was classified by comparing it with ROIs defined by the contours that capture 0.40 (40%) of the total blockade frequency of distributions acquired from pure protein solutions. Although the 0.40 integration contour was chosen specifically to minimize it, conflicts still arose with this classification scheme due to overlapping protein contours. The conflicts were resolved using a bootstrapping algorithm (see the Methods section in the Supporting Information).[44] Another pitfall in this kind of analysis has to do with normalization. If one protein is up-regulated while all the other proteins keep their expression, it is likely that all the other proteins will be detected as down-regulated without proper normalization. It should be possible to avoid this pitfall by adopting normalization schemes like those employed for RNA sequencing,[45] but in this analysis, it was assumed that all proteins were equally likely.

The results illustrated in Figure 3e were typical regardless of the contours, provided that they were chosen in the range from 0.20 to 0.70 (see Figure S16). According to this analysis, first of all, the relative abundance of CCL5 inferred from the blockade distributions for U937:MDA-MB-231 (1.3:1), and likewise, MDA-MB-231:MCF-7 was about 2- to 3-fold (after repeated testing), which was in line with the data acquired by simply integrating over the CCL5 domain (Figure S16). However, the CCL5 expression in MDA-MB-231 relative to MCF-7 fluctuated, likely due to phenotype diversity. Supposedly, luminal epithelial (CD326$^+$) cells constitute 99% of MCF-7 and about 70% of MDA-MB231.[42] Among these CD326$^+$ cells, 0.1% of MCF7 and 86% of MDA-MB-231 cells are cancer-initiating (CD44$^+$/CD24$^−$) cells, so there may be at least two distinct types of MDA-MB-231 cells. Second, both MMP1 and TIMP1 were expressed in both MDA-MB-231 and MCF-7, which was in line with prior work based on RT-PCR[46] and MS performed on conditioned medium.[47] In particular, the 3-fold relative abundance of TIMP1 in MDA-MB-231 compared to MCF-7 inferred from MS was corroborated by these single-cell and single-molecule nanopore measurements. Interestingly, PI3 (elafin) was tentatively identified in the blockade current distributions of all three cell types, whereas no PI3 was reported in MS spectra in either MDA-MB-231 or MCF-7.[47] Sensitivity to elafin is important because it is an elastase-specific inhibitor; its induction can be detrimental to human breast cancer cell viability and predicts survival. Interestingly, the rejected classification accounted for >10% of the total number of blockades in U937 and MDA-MB-231 for contours <0.60 and >40% in MCF-7 s regardless of the contour, which suggests that there are other low mass signatures to be discovered from these cell types, consistent with the idea that we are not

counting all of the proteins despite the limited window on the molecular volumes in the secretome.

Finally, by leveraging these observations, it was possible to dynamically and in real time discriminate cells by a specific molecular volume by using a commensurate detection window and filtering the blockade distribution accordingly (Figure 3f; top and middle). In this way, single secretions were identified in situ without amplification, delay, or further processing. The cumulative response within the detection window also allowed for the discrimination between cells secreting CCL5-like molecules in about 15 s (Figure 3f, bottom).

Conclusions. In conclusion, this pilot study demonstrated that it is feasible to detect and discriminate secretions from single cancer cells through the measurements of distinctive blockades associated with the translocation of single molecules through a nanopore. It was established that the distribution of blockades can be used to differentiate three different cancer cell lines (U937, MDA-MB-231, and MCF-7) quickly (<20 s). Importantly, the blockades associated with cancer biomarkers CCL5, PI3, TIMP1, and MMP1 were identified in the context of the secretome of these three cell types. Thus, this work delineated a method for single cell analysis that can be comprehensive in coverage and selective to a particular molecular volume, although it came with a cost: 15−20 s was required to discriminate a cell secreting a CCL5-like molecule. However, even with this throughput, precious primary samples could still be accommodated. Thus, this pilot study represents an important first step toward molecular diagnostics.

ASSOCIATED CONTENT

Ⓢ Supporting Information

The Supporting Information is available free of charge on the ACS Publications website at DOI: 10.1021/acs.nano-lett.8b01257.

Additional details on experimental methods and the electric field in a nanopore. Figures showing finite element simulations, nanopore current and topography, typical event rates, histograms, duration and fractional blockade distributions, detection and comparison of secretions, distribution estimation, hydrated structures, CCL5 sizing and gene expression, topography of pores and element simulations, RT-PCR results, and canvassing of multiple biomarkers. Tables showing computed volume estimates and typical finite element simulation parameters. (PDF)

AUTHOR INFORMATION

Corresponding Author

*E-mail: gtimp@nd.edu.

ORCID Ⓞ

Gregory Timp: 0000-0003-4418-5679

Author Contributions

§E.K. and M.H. contributed equally to the work

Notes

The authors declare no competing financial interest.

ACKNOWLEDGMENTS

REFERENCES

(1) Uhlén, M.; Fagerberg, L.; Hallström, B. M.; Lindskog, C.; Oksvold, P.; Mardinoglu, A.; Sivertsson, Å.; Kampf, C.; Sjöstedt, E.; Asplund, A.; Olsson, I.; Edlund, K.; Lundberg, E.; Navani, S.; Szigyarto, C. A.; Odeberg, J.; Djureinovic, D.; Takanen, J. O.; Hober, S.; Alm, T.; et al. Tissue-based map of the human proteome. *Science* **2015**, *347*, 1260419.

(2) Celis, J. E.; Gromov, P.; Cabezón, T.; Moreira, J. M.; Ambartsumian, N.; Sandelin, K.; Rank, F.; Gromova, I. Proteomic characterization of the interstitial fluid perfusing the breast tumor microenvironment: a novel resource for biomarker and therapeutic target discovery. *Mol. Cell. Proteomics* **2004**, *3*, 327−44.

(3) Ma, C.; Fan, R.; Ahmad, H.; Shi, Q.; Comin-Anduix, B.; Chodon, T.; Koya, R. C.; Liu, C. C.; Kwong, G. A.; Radu, C. G.; Ribas, A.; Heath, J. R. A clinical microchip for evaluation of single immune cells reveals high functional heterogeneity in phenotypically similar T cells,. *Nat. Med.* **2011**, *17*, 738−743.

(4) Mukherjee, P.; Mani, S. Methodologies to decipher the cell secretome. *Biochim. Biophys. Acta, Proteins Proteomics* **2013**, *1834*, 2226−32.

(5) Lu, Y.; Chen, J. J.; Mu, L.; Xue, Q.; Wu, Y.; Wu, P.-H.; Li, J.; Vortmeyer, A. O.; Miller-Jensen, K.; Wirtz, D.; Fan, R. High-throughput secretomics analysis of single cells to assess functional cellular heterogeneity. *Anal. Chem.* **2013**, *85*, 2548−2556.

(6) Hathout, Y. Approaches to the study of the cell secretome. *Expert Rev. Proteomics* **2007**, *4*, 239−48.

(7) Fujita, H.; Esaki, T.; Masujima, T.; Hotta, A.; Kim, S. H.; Noji, H.; Watanabe, T. M. Comprehensive chemical secretory measurement of single cells trapped in a micro droplet array with mass spectrometry. *RSC Adv.* **2015**, *5*, 16968.

(8) Chang, K.-P.; Lin, S.-J.; Liu, S.-C.; Yi, J.-S.; Chien, K.-Y.; Chi, L.-M.; Kao, H.-K.; Liang, Y.; Lin, Y.-T.; Chang, Y.-S.; Yu, J.-S. Low-molecular-mass secretome profiling identifies HMGA2 and MIF as prognostic biomarkers for oral cavity squamous cell carcinoma. *Sci. Rep.* **2015**, *5*, 11689.

(9) Wells, G.; Prest, H.; Russ, C. W. Why use signal-to-noise as a measurement of MS performance when it is often meaningless. *Agilent Application Note 5990−8341EN*. (**2011**). See https://www.agilent.com/cs/library/technicaloverviews/public/5990-8341EN.pdf (accessed June 10, 2018).

(10) Chen, S.-T.; Pan, T.-L.; Juan, H.-F.; Chen, T.-Y.; Lin, Y.-S.; Huang, C.-M. Breast Tumor Microenvironment: Proteomics Highlights the Treatments Targeting Secretome. *J. Proteome Res.* **2008**, *7*, 1379−1387.

(11) Chandramouli, K.; Qian, P.-Y. Proteomics: challenges, techniques and possibilities to overcome biological sample complexity. *Hum. Genomics Proteomics* **2009**, *2009*, 239204.

(12) Savaryn, J. P.; Catherman, A. D.; Thomas, P. M.; Abecassis, M. M.; Kelleher, N. L. The emergence of top-down proteomics in clinical research. *Genome Med.* **2013**, *5*, 53.

(13) Freedman, K. J.; Jürgens, M.; Prabhu, A.; Ahn, C. W.; Jemth, P.; Edel, J. B.; Kim, M. J. Chemical, thermal, and electric field induced unfolding of single protein molecules studied using nanopores. *Anal. Chem.* **2011**, *83*, 5137−44.

(14) Oukhaled, A.; Cressiot, B.; Bacri, L.; Pastoriza-Gallego, M.; Betton, J.-M.; Bourhis, E.; Jede, R.; Gierak, J.; Auvray, L.; Pelta, J. Dynamics of completely unfolded and native proteins through solid-state nanopores as a function of electric driving force. *ACS Nano* **2011**, *5*, 3628–38.

(15) Plesa, C.; Kowalczyk, S. W.; Zinsmeester, R.; Grosberg, A. Y.; Rabin, Y.; Dekker, C. Fast Translocation of Proteins through Solid State Nanopores. *Nano Lett.* **2013**, *13*, 658–663.

(16) Kennedy, E.; Dong, Z.; Tennant, C.; Timp, G. Reading the primary structure of a protein with 0.07 nm³ resolution using a sub-nanometre-diameter pore. *Nat. Nanotechnol.* **2016**, *11*, 968–976.

(17) Niedzwiecki, D. J.; Grazul, J.; Movileanu, L. Single-molecule observation of protein adsorption onto an inorganic surface. *J. Am. Chem. Soc.* **2010**, *132*, 10816–10822.

(18) Winter, J.; Ilbert, M.; Graf, P. C. F.; Özcelik, D.; Jakob, U. Bleach Activates A Redox-Regulated Chaperone by Oxidative Protein Unfolding. *Cell* **2008**, *135*, 691–701.

(19) Kurz, V.; Nelson, E. M.; Shim, J.; Timp, G. Direct Visualization of Single-Molecule Translocations through Synthetic Nanopores Comparable in Size to a Molecule. *ACS Nano* **2013**, *7*, 4057–4069.

(20) Kurz, V.; Tanaka, T.; Timp, G. Single cell transfection with single molecule resolution using a synthetic nanopore. *Nano Lett.* **2014**, *14*, 604–611.

(21) Zhou, M.; Liu, H.; Venkiteshwaran, A.; Kilduff, J.; Anderson, D. G.; Langer, R.; Belfort, G. High throughput discovery of new fouling-resistant surfaces. *J. Mater. Chem.* **2011**, *21*, 693–704.

(22) Peterman, E. J. G.; Gittes, F.; Schmidt, C. F. Laser-Induced Heating in Optical Traps. *Biophys. J.* **2003**, *84*, 1308–1316.

(23) Jaffe, L. On the concentration gradient across a spherical source washed by a slow flow. *Biophys. J.* **1965**, *5*, 201–210.

(24) Holliday, D. L.; Speirs, V. Choosing the right cell line for breast cancer research. *Breast Cancer Res.* **2011**, *13*, 215.

(25) Lehmann, M. H.; Schreiber, S.; Vogelsang, H.; Sigusch, H. H. Constitutive expression of MCP-1 and RANTES in the human histiocytic lymphoma cell line U-937. *Immunol. Lett.* **2001**, *76*, 111–3.

(26) Raillon, C.; Granjon, P.; Graf, M.; Steinbock, L. J.; Radenovic, A. Fast and automatic processing of multi-level events in nanopore translocation Experiments. *Nanoscale* **2012**, *4*, 4916–4924.

(27) Qin, Z. P.; Zhe, J. A.; Wang, G. X. Effects of particle's off-axis position, shape, orientation and entry position on resistance changes of micro-Coulter counting devices. *Meas. Sci. Technol.* **2011**, *22*, 045804.

(28) Székely, G. J.; Rizzo, M. L. A new test for multivariate normality. *J. Multivariate Analysis* **2005**, *93*, 58–80.

(29) Haridasan, N.; Kannam, S. K.; Mogurampelly, S.; Sathian, S. P. Translocation Mobilities of Proteins in Nanopores: A Coarse-Grained Molecular Dynamics Study. **2018**, arXiv:1801.08697v1. arXiv.org e-Print archive. https://arxiv.org/abs/1801.08697 (accessed June 10, 2018).

(30) Dimitrov, V.; Mirsaidov, U.; Wang, D.; Sorsch, T.; Mansfield, W.; Miner, J.; Klemens, F.; Cirelli, R.; Yemenicioglu, S.; Timp, G. Nanopores in solid-state membranes engineered for single molecule detection. *Nanotechnology* **2010**, *21*, 065502.

(31) Lv, D.; Zhang, Y.; Kim, H.-J.; Zhang, L.; Ma, X. CCL5 as a potential immunotherapeutic target in triple-negative breast cancer. *Cell. Mol. Immunol.* **2013**, *10*, 303–310.

(32) Hirata, B. K. B.; Oda, J. M. M.; Guembarovski, R. L.; Ariza, C. B.; de Oliveira, C. E. C.; Watanabe, M. A. E. Molecular Markers for Breast Cancer: Prediction on Tumor Behavior. *Disease Markers* **2014**, 1 DOI: 10.1155/2014/513158.

(33) Feizi, A.; Banaei-Esfahani, A.; Nielsen, J. HCSD: the human cancer secretome database. *Database* **2015**, *2015*, 1–8.

(34) Monastero, R. N.; Pentyala, S. Cytokines as Biomarkers and Their Respective Clinical Cutoff Levels. *Int. J. Inflammation* **2017**, *2017*, 4309485.

(35) Erickson, H. P. Size and Shape of Protein Molecules at the Nanometer Level Determined by Sedimentation, Gel Filtration, and Electron Microscopy. *Biol. Proced. Online* **2009**, *11*, 32–51.

(36) Nelson, E. M.; Kurz, V.; Shim, J.; Timp, W.; Timp, G. Using a Nanopore for Single Molecule Detection and Single Cell Transfection. *Analyst* **2012**, *137*, 3020–3027.

(37) Wang, X. C.; Watson, C.; Sharp, J. S.; Handel, T. M.; Prestegard, J. H. Oligomeric structure of the chemokine CCL5/RANTES from NMR, MS, and SAXS data. *Structure* **2011**, *19*, 1138–1148.

(38) Theoretical and Computational Biophysics Group. http://www.ks.uiuc.edu/Development/MDTools/molvolume/ (accessed June 10, 2018).

(39) Grubmüller, H. *Theoretical Biophysics Group, Institut für Medizinische Optik*; Ludwig-Maximilians-Universität München: München, Germany, https://www.mpibpc.mpg.de/grubmueller/solvate (accessed June 10, 2018).

(40) Ho, C.; Qiao, R.; Heng, J. B.; Chatterjee, A.; Timp, R. J.; Aluru, N.; Timp, G. Electrolytic Transport through a Synthetic Nanometer-Diameter Pore. *Proc. Natl. Acad. Sci. U. S. A.* **2005**, *102*, 10445–10450.

(41) Yin, H.; Glass, J. The phenotypic radiation resistance of CD44+/CD24(-or low) breast cancer cells is mediated through the enhanced activation of ATM signaling. *PLoS One* **2011**, *6*, e24080.

(42) Zhang, Y.; Yao, F.; Yao, X.; Yi, C.; Tan, C.; Wei, L.; Sun, S. Role of CCL5 in invasion, proliferation and proportion of CD44+/CD24- phenotype of MCF-7 cells and correlation of CCL5 and CCR5 expression with breast cancer progression. *Oncol. Rep.* **2009**, *21*, 1113–1121.

(43) Sumiya, Y.; Ishikawa, M.; Inoue, T.; Inui, T.; Kuchiike, D.; Kubo, K.; Uto, Y.; Nichikata, T. Macrophage Activation Mechanisms in Human Monocytic Cell Line-derived Macrophages. *Anticancer Res.* **2015**, *35*, 4447–4452.

(44) Efron, B.; Tibshirani, R. J. *An Introduction to the Bootstrap*; Chapman and Hall/CRC: New York, 1994.

(45) Li, J.; Witten, D. M.; Johnstone, I. M.; Tibshirani, R. Normalization, testing, and false discovery rate estimation for RNA-sequencing data. *Biostatistics* **2012**, *13*, 523–538.

(46) Bartsch, J. E.; Staren, E. D.; Appert, H. E. Matrix Metalloproteinase Expression in Breast Cancer. *J. Surg. Res.* **2003**, *110*, 383–392.

(47) Ziegler, Y. S.; Moresco, J. J.; Yates, J. R., III; Nardulli, A. M. Integration of Breast Cancer Secretomes with Clinical Data Elucidates Potential Serum Markers for Disease Detection, Diagnosis and Prognosis. *PLoS One* **2016**, *11*, e0158296.